

Heat transfer enhancement in wavy falling films studied by laser-induced fluorescence

Romain Collignon, Ophélie Caballina, Fabrice Lemoine, Christos N Markides, Guillaume Castanet

▶ **To cite this version:**

Romain Collignon, Ophélie Caballina, Fabrice Lemoine, Christos N Markides, Guillaume Castanet. Heat transfer enhancement in wavy falling films studied by laser-induced fluorescence. International Journal of Heat and Mass Transfer, 2023, 202, pp.123690. 10.1016/j.ijheatmasstransfer.2022.123690 . hal-03876985

HAL Id: hal-03876985
https://hal.science/hal-03876985

Submitted on 29 Nov 2022

HAL is a multi-disciplinary open access archive for the deposit and dissemination of scientific research documents, whether they are published or not. The documents may come from teaching and research institutions in France or abroad, or from public or private research centers.

L'archive ouverte pluridisciplinaire **HAL**, est destinée au dépôt et à la diffusion de documents scientifiques de niveau recherche, publiés ou non, émanant des établissements d'enseignement et de recherche français ou étrangers, des laboratoires publics ou privés.



Distributed under a Creative Commons Attribution - NonCommercial - NoDerivatives 4.0 International License

Heat transfer enhancement in wavy falling films studied by laser-induced fluorescence

R. Collignon[1,2*], O. Caballina[2], F. Lemoine[2], C.N. Markides[3] and G. Castanet[2]

[1] *Université Savoie Mont Blanc, CNRS, LOCIE, 73000 Chambéry, France*
[2] *Université de Lorraine, CNRS, LEMTA, 54000 Nancy, France*
[3] *Clean Energy Processes (CEP) Laboratory, Department of Chemical Engineering, Imperial College London, London SW7 2AZ, UK*

[*] *Corresponding author*

Abstract

The characteristics of thin liquid films flowing down a uniformly heated and inclined plane are investigated, with heat transfer across the wavy films quantified using up-to-date optical measurement techniques based on laser-induced fluorescence (LIF). A planar two-colour LIF technique provides the temperature distribution inside the films, but requires a high degree of wave regularity for the spatial reconstruction. A pointwise adaptation of the aforementioned technique, with much finer temporal sampling, provides simultaneous measurements of the average temperature over the film height and of the film thickness. Despite the loss of spatial resolution, the latter technique can be applied to diverse situations, especially when the waves lose their regularity and have large amplitudes. With these two approaches, the enhancement of heat transfer due to surface waves is traced along the film flow. A growing thermal boundary layer is found close to the inlet of the flow (i.e., first few cm), but its thickness remains small relative to the film thickness. Therefore, the heat transfer coefficient (HTC) is observed to be insensitive to the shape and amplitude of the waves at the free surface. A critical distance is necessary for the thermal boundary layer to be thick enough to interact with the flow structures associated with the waves, and the critical length scales with the Peclet number of the flow based on the specific flow rate. Several experiments are conducted to quantify the influence of the main flow parameters that control the HTC, such as the Reynolds number, the inclination angle and the wave frequency. For moderate wave amplitudes, the internal structure of the film is insensitive to the wave dynamics, and the temperature distribution is essentially dominated by thermal diffusion in the direction normal to the heated wall. Classical Nusselt theory is found to be applicable to the unperturbed (flat) film flows with some limited adjustments to predict the heat transfer rate. However, for the waves that have a larger amplitude, the classical Nusselt theory diverges from the experimental results. A sharp increase of the HTC by several tens of percent is observed over just a few cm, compared to an equivalent undisturbed liquid film with the same Reynolds number. Refined images of the temperature field are then used to better understand the mechanisms by which heat transfer is enhanced. Mixing appears in regions close to the wave front, then progressively extends to other film regions, tending to make the temperature more homogeneous. This has a strong effect on the local HTC in the troughs of the waves, with deviations of up to 40% relative to the flat film theory. Finally, a loss of wave regularity, observed after a few tens of cm from the inlet, accelerates the mixing by further altering the distribution of the temperature field over the entire liquid domain.

Nomenclature

Operators

$\Delta(\bullet)$	Difference
$\overline{(\bullet)}$	Time average
$(\bullet)^*$	Dimensionless parameter

Physical properties

α	Thermal diffusivity
λ	Thermal conductivity
ν	Kinematic viscosity
g	Gravitational acceleration
s	Temperature sensitivity of fluorescence signal

Variables

β	Wall inclination
δ	Film thickness
η	Efficiency factor
Γ	Specific flow rate
Nu	Nusselt number
Pe	Peclet number
Pr	Prandtl number
Re	Reynolds number
θ	Reduced temperature
φ	Phase of the wave
F	Fluorescence intensity
f	Perturbation frequency
h	Heat transfer coefficient
l	Flow width
q_v	Liquid flow rate
q_w	Wall heat flux density
T	Temperature
t	Time
t_0	Time period of the wave
u	Velocity
x	Film flow direction
z	Wall normal direction

Subscripts

0	Value obtained from Nusselt theory
m	Flow weighted average
max	Maximum
min	Minimum
ref	Reference
s	Surface
v	Volume average
i	Initial

1 Introduction

Falling liquid films are widely used in many industrial applications, which involve cooling, condensation, evaporation, and adsorption processes. The advantages of falling liquid films include high heat and mass transfer rates at relatively low liquid flow rates and short contact time between the liquid and solid wall. While the heat transfer is enhanced by the turbulence effects at high Reynolds number, for the low Reynolds numbers, the heat transfer coefficient is mainly enhanced by the interfacial instabilities that develop on the film surface. Some investigators found that the waviness of laminar liquid films can enhance heat transfer in very large extend (up to 80% in Miyara (1999)). However, there is still a need to understand and predict the enhancement mechanism, despite numerous theoretical (Demekhin et al., 2007; Dietze et al., 2008; Albert et al., 2014; Chhay et al., 2017), numerical (Yu et al., 2013; Miyara, 1999) and experimental (Markides et al., 2016; Kabov et al., 2002) studies that have been dedicated to this topic.

Film flow can be divided into several regions (Figure 1). Large lumps of liquid are carrying major amount of liquid mass forming large 2D or 3D wave region (Charogiannis et al., 2017; Denner et al., 2018). Besides these large waves, capillary waves with smaller amplitudes are slowly moving and are progressively overtaken by the larger waves. In the remaining inter-wave region, a rather thin film can exist between the wave tail and the beginning of the next wave. When the wave amplitude becomes significant, only a small amount of liquid mass is transported within the thin film region. Viscous and thermal boundary layer are periodically destructed under the wave and is recovered in the inter-

wave region (Brauner and Marón, 1983). Some authors pointed out that the recirculation zones in the large wave region is the place of an intense mixing between the colder liquid and heated liquid coming from the thermal boundary layer (Roberts and Chang, 2000; Rastaturin et al., 2006; Albert et al., 2014). The size of these recirculation zones, however, is depending on the wave amplitude and the wavelength (Gao et al., 2003). Other authors suggested that the non-linearity of the velocity profile with the distance to the wall could be an enhancement factor for the heat transfer. As surface undulations are considered, the mean thickness of the film gets smaller (Zhou and Prosperetti, 2020), which leads to a reduction of the resistance to thermal conduction through the liquid film. Recently, direct numerical simulations highlighted the role of flow separation occurring in the capillary troughs ahead of the main wave front (Dietze et al., 2008; Dietze and Kneer, 2011). The rapid change in the direction of the streamlines induce an adverse pressure distribution, which can sometimes result in vortex formation in the capillary waves region close to the wall (Tihon et al., 2006; Dietze et al., 2008). The heat transport is mainly enhanced in the region between the capillary wave and the crest of the solitary wave (Schagen et al., 2006). As the temperature is not uniform in the liquid film and at its surface, important questions remain about the role that the thermo-capillary waves can play in deforming the liquid-gas interface as evidenced by Joo et al. (1996); Kabov et al. (2002) and Zaitsev and Kabov (2005).

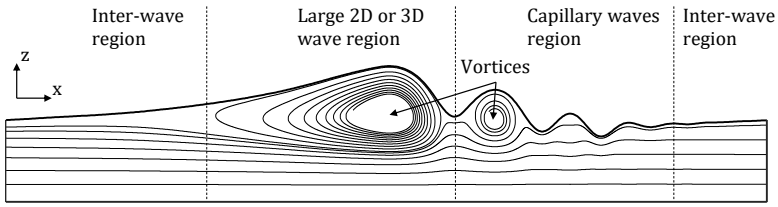


Figure 1: Topology of a wavy film with capillary waves flowing down an inclined plane.

Currently, in the absence of a complete and well-established theoretical framework, predicting the cooling performance is still very complex. Remaining questions about the heat transfer mechanisms warrant further experimental investigations. The present work is built upon our previous efforts to experimentally characterize the heat transfer in thin wavy liquid films. In Collignon et al. (2021), an imaging technique based on planar laser-induced fluorescence was developed to visualize the temperature field inside the waves, illuminating the film transversely with a thin laser sheet. Measurements revealed different levels of thermal mixing through which the liquid film is transiting when it is traversed by periodical waves. More recently, Collignon et al. (2022) developed another measurement technique based on laser-induced fluorescence. A cylindrical laser beam is directed onto the liquid film. From the intensity of the fluorescence signal, both the temperature and the liquid height can be inferred at the measurement point with a short time response and a sampling rate of several kHz. These two temperature measurements provide further insights into the heating process inside the liquid film, as they complement measurements at the liquid film surface performed with infrared cameras by several investigators in the past.

In this study, the LIF techniques mentioned above are used to access the heat transfer. Data are obtained changing the parameters influencing the liquid flow: the wall inclination, the liquid flow rate, and the wave frequency. In a first step, the analysis is simplified focusing on the time averaged values

of the liquid temperature for the evaluation of the Nusselt number and the heat transfer coefficient. Comparison to the classical solution of the Nusselt theory, valid for a smooth laminar film, is performed to identify the most favorable conditions for the heat transfer enhancement. Finally, a more detailed analysis is carried out to point out the regions playing a dominant role in the thermal mixing. The emphasis will be put on the main mechanisms responsible for heat transfer enhancement.

2 Theoretical model for heat transfer in a smooth liquid film

In order to describe the heat transfer enhancement in a thin liquid film, it is commonly referred to the case of a smooth liquid film of equivalent flow rate. The heat transfer characteristics in such a film can be derived from the Nusselt theory. The most relevant parameters are recalled in Figure 2. The wall is inclined with an angle β to the horizontal and a uniform heat flux density is applied at the wall.

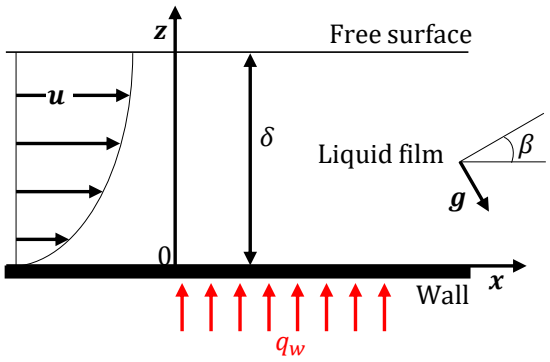


Figure 2: Parameters used for the flat liquid film model.

Given the rather low values of the Reynolds numbers, a parabolic velocity profile is considered inside the liquid film:

$$u(z) = \frac{g \cdot sin(\beta) \cdot \delta^2}{2\nu} \left(\frac{2z}{\delta} - \frac{z^2}{\delta^2} \right), \tag{1}$$

where $u(z)$ is the velocity component parallel to the wall and ν is the kinematic viscosity of the fluid. Using this expression of $u(z)$, the heat equation can be written as:

$$u(z) \frac{\partial T}{\partial x} = \alpha \left(\frac{\partial^2 T}{\partial x^2} + \frac{\partial^2 T}{\partial z^2} \right), \tag{2}$$

where α is the thermal diffusivity of the liquid. Introducing the dimensionless parameters (Davis, 1973):

$$x^* = \frac{x}{\delta \cdot Pe} \qquad z^* = \frac{z}{\delta} \qquad \theta^* = \frac{T - T_i}{q_w \frac{\delta}{\lambda}}, \tag{3}$$

with λ representing the thermal conductivity, the heat equation (2) can be rewritten as :

$$\left(2\, z^* - z^{*2} \right) \frac{\partial \theta^*}{\partial x^*} = \frac{\partial^2 \theta^*}{\partial z^{*2}}. \tag{4}$$

The Peclet number $\mathrm{Pe} = \mathrm{Re} \cdot \mathrm{Pr}$ compares the heat transfer by convection and by diffusion within the film. Presently, Pe is relatively high ($1000 \leq \mathrm{Pe} \leq 1800$), so the heat diffusion can be neglected

compared to the convective heat flux in the x direction, justifying the simplifications made in Equation (4). For the resolution, the following set of boundary conditions is prescribed:

$$\left.\frac{\partial \theta^*}{\partial z^*}\right|_{z^*=0} = -1 \qquad \left.\frac{\partial \theta^*}{\partial z^*}\right|_{z^*=1} = 0 \qquad \theta^*|_{x^*=0} = 0 \tag{5}$$

Figure 3 shows the solution to the above problem obtained numerically using the element finite method. On this figure, the white line corresponds to the thickness of the thermal boundary layer, defined as the points where the difference $(\theta^* - \theta^*_w)$ is equal to 90% of the whole temperature variation with the film thickness $(\theta^*_s - \theta^*_w)$. It is apparent that the thermal boundary layer is fully developed for $x^* \geq 0.05$, when its thickness stabilizes at an approximately constant value. For very large values of x^*, the temperature field gets established inside the film and follows a self-similar evolution with respect to x. The temperature gradient $\partial\theta^*/\partial x^*$ becomes a constant in Equation (4).

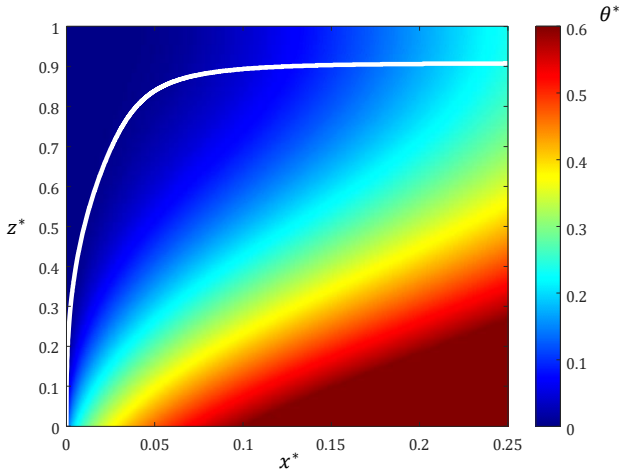


Figure 3: Growth of the thermal boundary layer (white line) superimposed to the solution of the theoretical Nusselt flat film solution represented in dimensionless variables under adiabatic condition at the free surface.

The heat transfer in the film is quantified introducing the Nusselt number Nu and the heat transfer coefficient h, which are defined as follows:

$$h = \frac{q_w}{\Delta T} \tag{6}$$

$$Nu = \frac{h\ \delta}{\lambda} \tag{7}$$

In the above expressions, ΔT is the temperature difference between the solid wall and the liquid film. While the temperature measured by the micro-thermocouples is the only possible choice for the wall temperature T_w, there are several possibilities for the temperature of the liquid film:

- In many theoretical and numerical studies, the average temperature weighted by the flow velocity (Chernyavskiy and Pavlenko, 2017; Wan et al., 2017; Huaylla et al., 2019) is preferred:

$$T_m(x) = \frac{\int_0^\delta u(z)\ T(x,z)\ dz}{\int_0^\delta u(z)\ dz} \tag{8}$$

Since the velocity field is not characterized in the present work, the Kapitza-Shkadov model (Shkadov, 1967) was implemented for the derivation of the velocity as described in Appendix A.1 using measured values of the film height.

- Alternatively, the volume average temperature T_v can be considered:

$$T_v(x,t) = \frac{1}{\delta(x,t)} \int_0^{\delta(x,t)} T(x,z,t)\, dz, \tag{9}$$

This temperature has the advantage of being directly obtained from the measurements with the LIF probe system or by integrating the temperature in the thickness direction in the PLIF images. Both techniques were presented in previous papers (Collignon et al., 2021, 2022) and will be briefly described later.

- In the literature, the surface temperature T_s at the liquid/air interface was also chosen in several experimental studies as it can be measured using an infrared camera (Chinnov et al., 2012; Mathie et al., 2013; Markides et al., 2016; Chinnov and Abdurakipov, 2017) or laser-induced fluorescence (Charogiannis et al., 2015; Charogiannis and Markides, 2019). In the present study, $T_s(x)$ can be determined from the PLIF images by retrieving the temperature value of the pixels close to the free surface.

The value of the Nusselt number depends on the choice of the film temperature considered to calculate ΔT. When the heat transfer through the film is established, recalling that $\partial\theta^*/\partial x^*$ is a constant, it can be easily demonstrated that the asymptotic limits for the Nusselt number are the following:

$$\begin{aligned} \lim_{x\to+\infty} Nu_{0,m}(x) &= 2, \\ \lim_{x\to+\infty} Nu_{0,s}(x) &= \frac{3}{2} \text{ and} \\ \lim_{x\to+\infty} Nu_{0,v}(x) &= \frac{5}{2}. \end{aligned} \tag{10}$$

where Nu_m, Nu_v or Nu_s are respectively the Nusselt numbers based on T_m, T_v and T_s. The index 0 denotes a flat film without any waves at its surface. In the transient region before the establishment of the thermal gradients, their evolution can be calculated based on the numerical resolution of Equation (4).

3 Experimental methods

3.1 Film-flow apparatus and procedure

The liquid film flows along a titanium foil (100 µm thick, 300 mm wide, and 400 mm long) that is stretched between two copper rods, also serving as electrodes to supply an electric current through the foil (Figure 4). The two copper electrodes are connected by a bundle of electrical cables to a DC power supply, which provides a current up to 1500 A for a 3 V voltage. The heat flux q_w generated by the electrical resistance in the foil, reaches up to 3.75 W/cm^2 and is distributed almost uniformly

over the foil surface. The foil, the two electrodes, and the upstream tank forms an assembly which is allowed to rotate with respect to the horizontal up to an inclination angle β of 45 °. The liquid film is generated by an overflow of the upstream tank. After flowing down the inclined wall, the liquid goes into the buffer tank, then it is pushed by a pump back to the upstream tank. A heat exchanger allows maintaining a constant liquid temperature T_i at the inlet of the upper tank. In the following, T_i is set to 10°C. Changing the inclination β of the titanium foil and the flow rate q_v allows adjusting the thickness δ of the film and the Reynolds number Re which is defined as :

$$\mathrm{Re} = \frac{\Gamma}{\nu}, \tag{11}$$

where $\Gamma = q_v/l$ is the liquid flow rate per unit width and ν is the kinematic viscosity of the liquid. The liquid flow rate q_v is measured by an ultrasonic flow-meter (measuring range 0 – 13 L/min). The falling film being extremely sensitive to external perturbations, the pump and the experimental setup were placed on vibration dampers. A honeycomb grid inside the upper reservoir insures a laminar flow and a uniform distribution of the liquid at the film inlet.

Instabilities can develop naturally at the film surface, however in the present study, these are forced using a loudspeaker placed above the upper tank. The membrane of the loudspeaker is connected to a plastic plate in contact of the water free surface in the upper tank. The vibration of the loudspeaker drives the plastic plate vertically, which generates a fluctuation of the flow rate and forces the onset of film instabilities at the outlet of the upper tank.

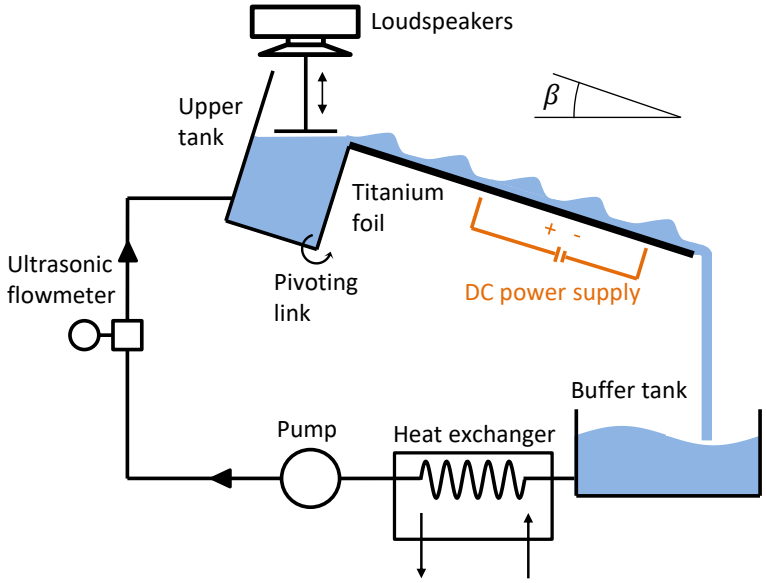


Figure 4: Set-up used for the generation of the waves and the heating of the falling liquid film.

3.2 Measurement techniques

Several measurement techniques were associated in order to characterize the heat transfer and the flow characteristics of the falling films.

3.2.1 Temperature measurements in the liquid film

The temperature of the liquid film is measured based on the two-color laser-induced fluorescence technique (Sakakibara and Adrian, 1999; Chaze et al., 2017; Stiti et al., 2019) which can be implemented to obtain either an image of the temperature distribution within the film or the volume average temperature in the film thickness. The liquid is seeded with fluorescent molecules in trace quantities (typically a few μg/L) and a laser beam is used to induce a fluorescence signal. The temperature response of many fluorescent dyes can be expressed as an exponential function of temperature (Chaze et al., 2016):

$$F = F_{ref} \cdot \exp\left(s \cdot (T - T_{ref})\right) \tag{12}$$

where F is the intensity of the fluorescence signal, which values F_{ref} at a reference temperature T_{ref}. The parameter s denotes the temperature sensitivity of the fluorescent signal, $s = F^{-1} \cdot dF/dT$. According to Chaze et al. (2016), s reaches a few percents per degree celcius for specific organic dyes such as fluorescein and kiton red. The wall in titanium and the electrodes do not offer any optical access. The fluorescence signal is thus detected from the above of the liquid film using a light detector. A ratiometric approach using two spectral bands of detection is adopted to determine the liquid temperature. Two dyes whose fluorescent emissions are shifted in wavelength, are mixed into the water solution and the intensity ratio of their fluorescence signal is calculated. The fluorescence signal depends on the temperature, the film thickness and the wave profile, but the dependencies on the film thickness and the wave profile can be eliminated by calculating the intensity ratio of the two detection bands.

Planar imaging

Collignon et al. (2021) applied the method to visualize the temperature field within thin liquid films. A laser sheet is directed on the liquid film as shown in Figure 5.a. The illuminated region of the film is observed by means of two CCD cameras in front of which optical filters are mounted to collect the fluorescence signal. The ratio of the camera images is converted into a temperature field. A special procedure, described by Collignon et al. (2021) is used to reconstruct the whole temperature field in the waves by assembling images taken at different times. In addition, optical distortions due to light refraction at the liquid/air interface were corrected.

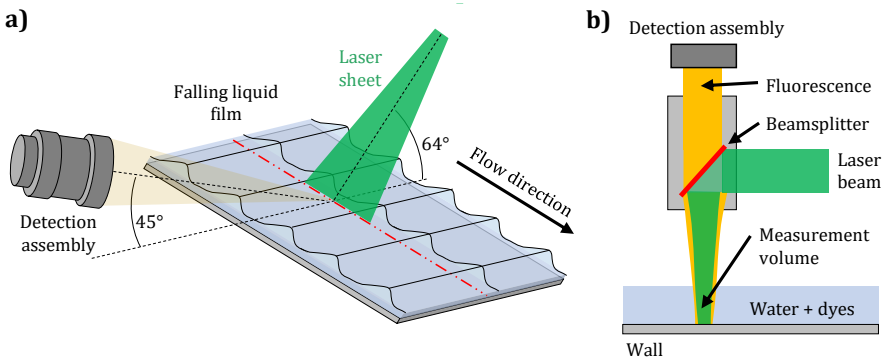


Figure 5: Optical configuration used for the LIF techniques applied to the falling film. a) Illumination by a laser sheet and detection by a camera assembly for the PLIF technique. b) Illumination and detection by the punctual LIF probe.

Film average temperature

The optical probe developed by Collignon et al. (2022), presented in Figure 5.b, enables measurement of the volume average temperature $T_v(x,t)$ as defined in Eq. (9). A continuous-wave laser is directed normal to the wall by the probe optics. The liquid film is illuminated through its entire thickness and the laser-induced fluorescence is collected by the same optical system. A combination of beam splitters and chromatic bandpass filters is used to separate the fluorescence signal in two spectral bands before the detection by two photomultiplier tubes and the calculation of the fluorescence ratio. Although this information could be extracted from the planar imaging technique described above, the probe requires much less optical alignment when changing the measurement position and is overall much more robust considering strongly deformed waves. The time response (of the order of ns) is well below the time period of the wave, which allows the temperature to be finely resolved in time during the wave passage.

3.2.2 Film thickness measurement

Beside the temperature, the height of the liquid film $\delta(x,t)$ is also measured with the LIF probe. Given that the depth of field of the collection optics is much larger than the thickness of the liquid film, the intensity of the fluorescent signal F is expected to be proportional to the film height δ. The thickness is measured simultaneously with the temperature of the film. A correction factor is thus introduced to account for the temperature variation of the fluorescence emission:

$$\delta = \delta_{ref}(T_{ref}) \cdot \frac{F(T)}{F_{ref}(T_{ref})} \cdot exp(-s \cdot (T - T_{ref})), \tag{13}$$

where s is the temperature sensitivity of the fluorescence signal in the detection band considered for the thickness measurement. Only relative variation of thickness can be determined from the LIF signal. To get a quantitative measurement of the film thickness, a reference intensity F_{ref} is measured under isothermal conditions on a smooth liquid film, when the film height is δ_{ref} and the temperature is T_{ref}.

As for a validation, comparisons between the planar imaging and the pointwise measurement techniques were carried out. An illustration is given in Figure 6 where the volume average temperature T_v and the thickness δ of the film are presented as a function of the phase of the wave φ. A good agreement is found for the most part of the wave profile. The wave height and the temperature variation are very similar. The slight differences can be attributed to the fact that those measurements were performed several days apart under experimental conditions that were probably not strictly the same.

3.2.3 Wall temperature measurement

The wall temperature T_w is measured using ten micro-thermocouples glued on the back side of the titanium foil. Their small diameter (130 µm) allows to have a time response very short in comparison to the wave period. The resistance to heat conduction is negligible within the titanium foil, given its 100 µm thickness. This means that the temperature is expected to be equal between the upper and lower sides of the wall. Figure 7 shows typical measurements of the wall temperature performed with one of the microthermocouples a few centimeters before the end of the wall ($x = 250$ mm). The thermal

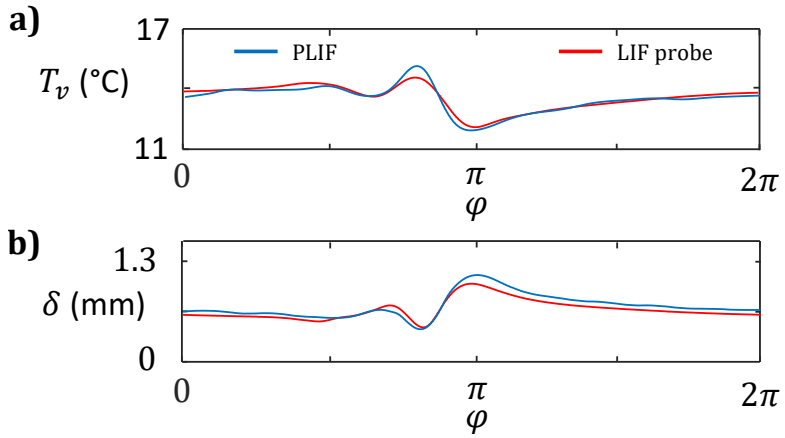


Figure 6: Comparison of the average temperature T_v (a) and the film height δ (b) measured with the PLIF technique and the LIF probe (Re = 200, $\beta = 10$ °, $x = 160$ mm, $f = 10$ Hz, $T_i = 10$ °C and $q_w = 1.25$ W/cm^2).

response was recorded for several wave frequencies. In all cases, the temperature fluctuations are rather small, on the order of 0.2°C. Similar observations were reported in studies where IR thermography was used for monitoring the wall temperature. In particular, comparable experiments also using a thin electrically heated titanium foil, were carried out by Al-Sibai et al. (2002) and Mathie et al. (2013). In Figure 7.b, a Fast Fourier transform of the thermocouple responses is performed. Only for $f = 3$ Hz, a component at the wave frequency can be pointed out in the measurements. For larger wave frequencies, namely $f = 7$ Hz and 10 Hz, the fluctuations are indistinguishable from a white noise. Typically, the standard deviation of the wall temperature measurements is of the order of 0.1°C. The wall temperature is thus considered constant in time.

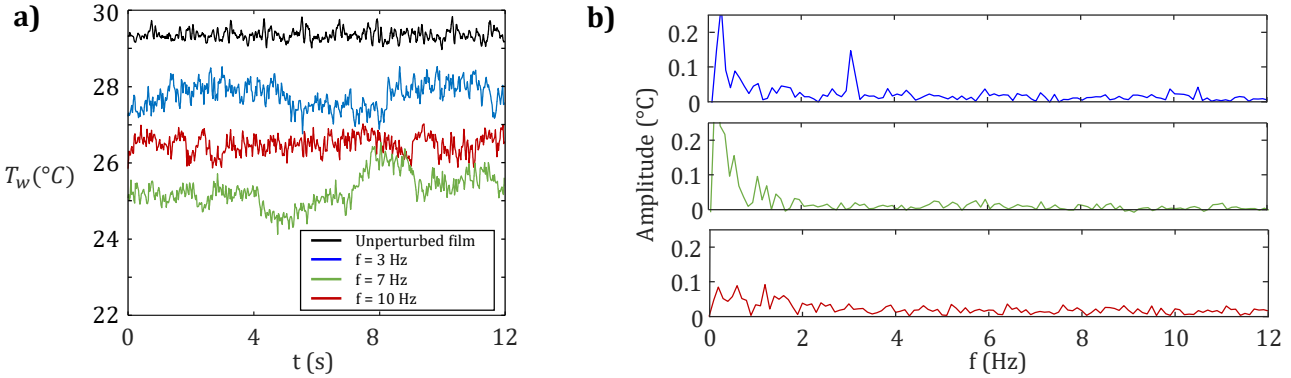


Figure 7: Variations in wall temperature during the passage of waves at different frequencies measured with Re = 200, $\beta = 10$ °, $x = 250$ mm, $T_i = 15$ °C and $q_w = 1.25$ W/cm^2. Raw data are presented in (a) and their corresponding FFT are presented in (b). The difference in wall temperature between the different cases is a consequence of heat transfer.

4 Results and discussion

The experimental techniques, presented earlier, were used to characterise the heat transfer in the film in different flow configurations. Parameters such as the liquid flow rate, the angle of the solid wall, as well as the wave frequency, were examined in more details since they are well known to play a role in

the development of wave instabilities. As illustrated in the following, observations must be conducted at different scales to gain a better understanding of the phenomena. From measurements at a fixed location, it is possible to obtain useful information about the temperature change as the wave passes through the measurement volume, which can provide insight into the mechanism of heat transfer enhancement. On the other hand, less refined measurements made at different locations can provide information on the increase of the wall and liquid temperatures with the downstream distance. These measurements make it possible to evaluate the overall heat exchange in order to compare different flow configurations and different type of perturbations.

4.1 Wave amplitude and flow characteristics

Hydrodynamic fluctuations and heat transfer are strongly correlated. Therefore, the characteristics of the flow and especially those of the surface waves must be known precisely for each parameter considered in the study. Generally speaking, the response of the liquid film to the loudspeaker perturbation is a complex function of the perturbation frequency f and the liquid flow rate q_v. Figure 8 shows the wave amplitudes for different values of f and Re. The depth of the troughs δ_{min} and the height of the main bumps δ_{max} are normalized by the average film thickness $\overline{\delta}$. Depending on the frequency, the vertical motion transmitted to the free surface is more or less dampened inside of the upstream tank. The frequency of 7 Hz is clearly the one that allows generating waves of the largest height. After leaving the upstream tank, the waves are in constant evolution. For $f = 3$ Hz, δ_{max} grows very slowly in the first half of the wall ($x < 150$ mm). Then, δ_{max} increases significantly until the end of the wall but δ_{min} remains quite high. For $f = 7$ Hz, the difference $(\delta_{max} - \delta_{min})$ remains about constant with the downstream distance x (Figure 9). The depth of the troughs δ_{min} and the height of the humps δ_{max} are both increasing at a constant rate. For $f = 10$ Hz, the wave front evolves quite differently. At the outlet of the upstream tank, the wave amplitude is small. Values of δ_{min} and δ_{max} are comparable to the cases at $f = 3$ Hz. A rapid decrease of δ_{min} and increase of δ_{max} is observed until about x =180 mm. At this position, the wave characteristics approaches those of the film at 7 Hz. After $x = 180$ mm, the maximum height of the humps δ_{max} falls drastically while δ_{min} starts to increase very slightly. The reason for this evolution is not clear. A closer look at the measurements reveals that the wave profile is shifting towards multiple troughs in front of the main wave. For all the frequencies considered, the shape of the waves does not stabilize before the end of the heating wall. The trends described above are globally the same for the three tested values of Re. In general, decreasing Re tends to slightly increase δ_{min} and δ_{max}.

The angle β of the wall with the horizontal also has an effect on the wave amplitude. In most of the cases, the wave amplitude increases with β, but the opposite is sometimes also observed (Figure 9). Whatever the angle β, the wave amplitude remains predominantly correlated with the wave frequency, meaning that the amplitudes are sorted in the same order with respect to the wave frequency for all the β values tested in our experiments.

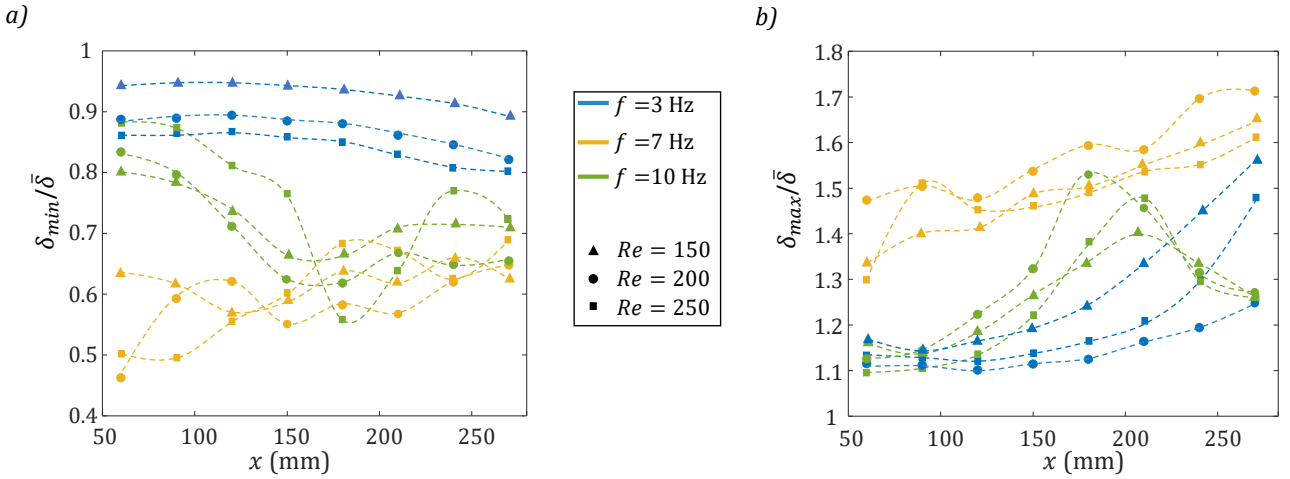


Figure 8: Evolutions of the minimum (a) and maximum (b) of the film thickness as a function of the distance x from the flow inlet. Measurements obtained with the LIF probe for three values of the Reynolds number: Re = 150 (△), Re = 200 (◯) and Re = 250 (□), and $\beta = 10$ °, $T_i = 10$ °C and $q_w = 1.25$ W/cm^2. The dotted curves were hand drawn to help reading.

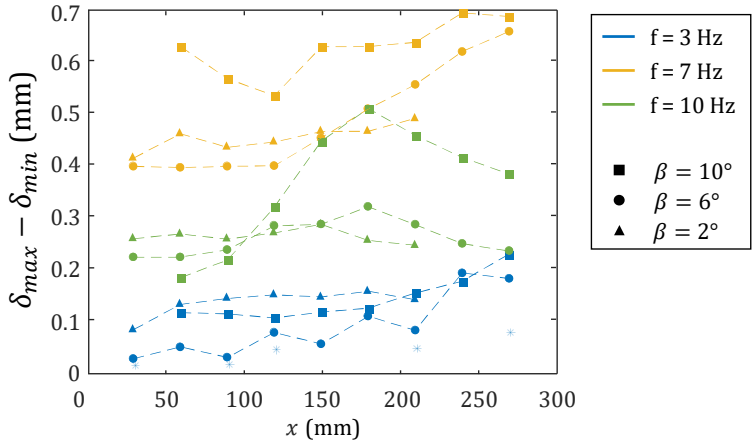


Figure 9: Spatial evolution of the amplitude of the waves for three perturbation frequency $f = 3$ Hz, $f = 7$ Hz and $f = 10$ Hz represented along the flow distance x. The measurements are represented for Re = 200 and $q_w = 1.25$ W/cm^2. The dotted curves were hand drawn to help reading.

4.2 Global heat transfer

In this section, heat transfer characteristics are analysed using temperatures that are averaged over the duration of the wave period. The upper bar symbol ($\bar{\bullet}$) denotes a quantity that is averaged temporally over the period t_0 of a wave:

$$\overline{T}(x) = \frac{1}{t_0} \int_{t_0} T(x,t)\, dt. \tag{14}$$

From an argument of energy conservation, the time-averaged temperature of the liquid film is expected to increase linearly with the downstream distance x, due to the fact that heat produced by the electrical current inside the titanium foil is almost completely dissipated in the liquid film. Only a negligible part of the heat is transferred directly to the air at the lower side of the wall and the cooling effect due to liquid evaporation can be neglected for the moderately low temperatures considered in our experiments. Figure 10 confirms that the volume-averaged temperature $\overline{T_v}$ follows a linear trend.

Furthermore, measurements obtained for $\overline{T_v}$ at different wave frequencies are superimposed when the same heat flux density q_w is applied to the wall. In Figure 10, the volume average temperature $\overline{T_v}$ is also evaluated using both the LIF proble and the PLIF technique. Here also, Here also, it is possible to verify that the two methods used to measure the temperature of the liquid are in perfect agreement. On Figure 10, the wall temperature measured using thin thermocouples is also displayed for comparison with the temperature in the liquid film. As expected, the wall temperature T_w is always above the liquid film temperature $\overline{T_v}$. In the first centimetres (typically for x<50 mm), T_w increases rapidly with x, then the difference ΔT in temperature between the liquid film and the wall stabilizes progressively around 8°C. In the absence of perturbation (no wave generation), ΔT becomes a constant for $x > 200$ mm, as the temperature gradients get established inside the liquid film.

When a perturbation is applied, a critical distance $x_{crit} \approx 100$ mm is required to detect an effect of the waves on the wall temperature T_w. Beyond this distance, the wall temperature grows at a much slower pace and eventually decreases, due to a better cooling efficiency by the liquid film. This effect is more pronounced for the case $f = 7$ Hz which has the largest wave height among the tested conditions. For $f = 3$ Hz, the amplitude of the wave is very small and the evolution of the wall temperature T_w is not distinct from that of an unperturbed liquid film evaluated by the Nusselt theory.

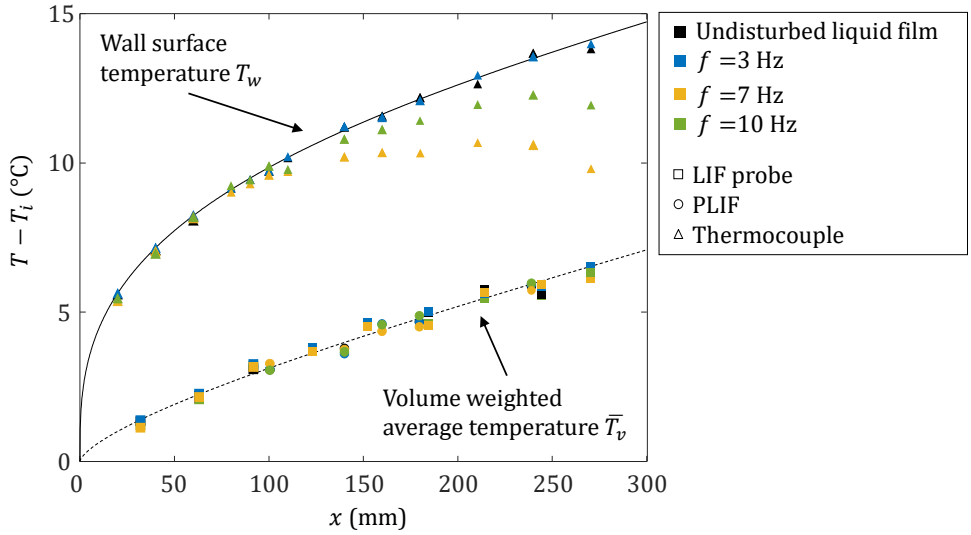


Figure 10: Spatial evolution of the volume weighted average temperature of the liquid film $\overline{T_v}$ and T_w the wall surface temperature. Comparison to the theoretical model for the undisturbed flat liquid film in dotted and solid lines respectively, with Re = 200, $\beta = 10$ ° and $q_w = 1.25$ W/cm^2.

In order to quantify the heat transfer enhancement, the Nusselt number $\overline{\mathrm{Nu}}$ determined experimentally can be used. An efficiency factor η can be introduced as followed:

$$\eta = \frac{\overline{\mathrm{Nu}}}{\mathrm{Nu}_0}. \tag{15}$$

In this expression, Nu_0 corresponds to the Nusselt number of the unperturbed liquid film with the same liquid flow rate. Nu_0 can be valuated using the Nusselt theory. However, different values of the Nusselt number can be obtained depending on the film temperature considered for the calculation of ΔT. In Equation (7), different values of Nu_0 were obtained considering the surface temperature T_s, the average temperature weighted by the flow velocity T_m and the volume average temperature T_v are

considered. This raises questions regarding the possibility of having different values of the efficiency η for each of these three temperatures. To address this question, T_m, T_v and T_s will be evaluated from the experimental temperature field measured by the PLIF technique. Then, the obtained temperatures will be used to calculate and compare the Nusselt number and the efficiency factor with these three definitions of ΔT.

4.2.1 Experimental characterisation of the Nusselt number

In a first stage, it was verified that the values of T_m, T_v and T_s extracted from the temperature fields measured by the PLIF technique, were sufficiently accurate to provide acceptable values of Nu_m, Nu_v and Nu_s. These tests were performed on a film undergoing a weak perturbation at the frequency of $f = 3$ Hz. Figure 11.a shows the spatial evolutions of $\overline{T}_m$, $\overline{T}_v$ and $\overline{T}_s$ for the same flow conditions as in Figure 10, i.e. Re = 200, $\beta = 10°$ and $q_w = 1.25$ W/cm^2 and in the case of a wave frequency $f = 3$ Hz, which causes little disturbance to the liquid film. The surface temperature T_s is lower because the film surface is the region the most distant from the heating surface. The velocity u tends toward 0 close to the wall due to the no slip condition. As a result, the wall temperature has less weight in the evaluation of $\overline{T}_m$ than in the one of $\overline{T}_v$. As shown in Figure 11.a, $\overline{T}_m$ is always lower than $\overline{T}_v$. From these experimental results, a time-averaged value of the Nusselt number can be calculated by evaluating the ratio of the time-averaged film thickness $\overline{\delta}$ and the time-averaged $\overline{\Delta T}$. Another approach is to evaluate directly the time-averaged value of the ratio, i.e. $\overline{(\delta/\Delta T)}$. Although these two methods are not equivalent, they give very comparable results as demonstrated in Appendix A.2 for a few example cases. Figure 11.b shows that $\overline{\mathrm{Nu}}$ is decreasing with the distance x. As a thermal boundary layer develops within the liquid film starting from $x = 0$, the temperature gradients are decreasing inside the film. Experimental values of $\overline{\mathrm{Nu}}_m$, $\overline{\mathrm{Nu}}_v$ and $\overline{\mathrm{Nu}}_s$ are consistent with the predictions of the Nusselt theory. In particular, at the end of the wall, experimental values of the Nusselt number get close to the theoretical asymptotic limits given in Equation (10). This good agreement is achieved due to the low wave height at $f = 3$ Hz. This agreement also supports the assumptions made earlier in the model of negligible thermal losses to the ambient atmosphere from the lower surface of the titanium foil and the upper surface of the liquid film.

4.2.2 Influence of the waviness

To evidence the effect of the film waviness, the wave frequency f was changed from 3 Hz to 10 Hz, while maintaining a fixed Reynolds number Re = 200 and a fixed wall inclination $\beta = 10$ °. Figure 12 shows the evolution of $\overline{\mathrm{Nu}_v}$ and $\eta_v = \overline{\mathrm{Nu}_v}/Nu_{0,v}$ as a function of the downstream distance x. In Fig. 12, fictional points were added at $x = 50$ mm for an efficiency factor $\eta_v = 1$ to help read the figure. The position of the fictional point was motivated by the results presented in Fig. 10, were every measurement corresponds to the Nusselt solution for $x <= 50$ mm. As expected, on Fig. 12, η_v is always close to 1 for $f = 3$ Hz, since the wave amplitude is very small. The efficiency factor η_v reaches its largest value (about 40%) at the end of the heated wall for the configuration with the largest wave height at $f = 7$ Hz. The heat transfer is getting more and more efficient with the downstream distance x, which is probably a sign that the thermal mixing is expanding within the liquid film promoting greater heat transfer. For an intermediate wave amplitude ($f = 10$ Hz), the heat transfer enhancement is only 10% and it is also observed that η_v is increasing at a much lower rate with the distance x.

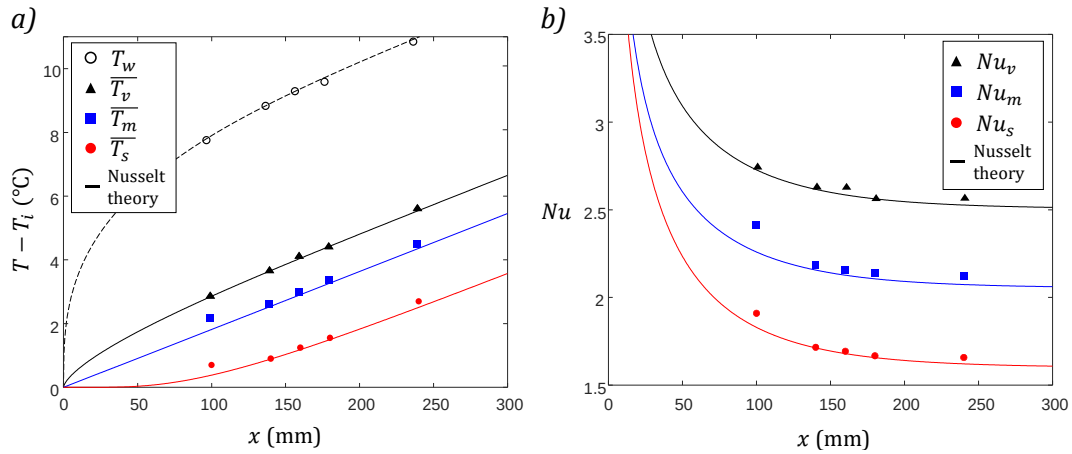


Figure 11: Spatial evolution of the time-averaged values of the temperatures $\overline{T}_m$, $\overline{T}_v$ and $\overline{T}_s$ (a) and their corresponding values of the Nusselt number: $\overline{\mathrm{Nu}}_m$, $\overline{\mathrm{Nu}}_v$ and $\overline{\mathrm{Nu}}_s$ (b). Measurements, in dots, are provided by PLIF images of the temperature field inside a film generated in the conditions: $f = 3$ Hz, for $\mathrm{Re} = 200$, $\beta = 10$ ° and $q_w = 1.25$ W/cm^2. The lines are extracted from the Nusselt theory in the same configuration as the experiments.

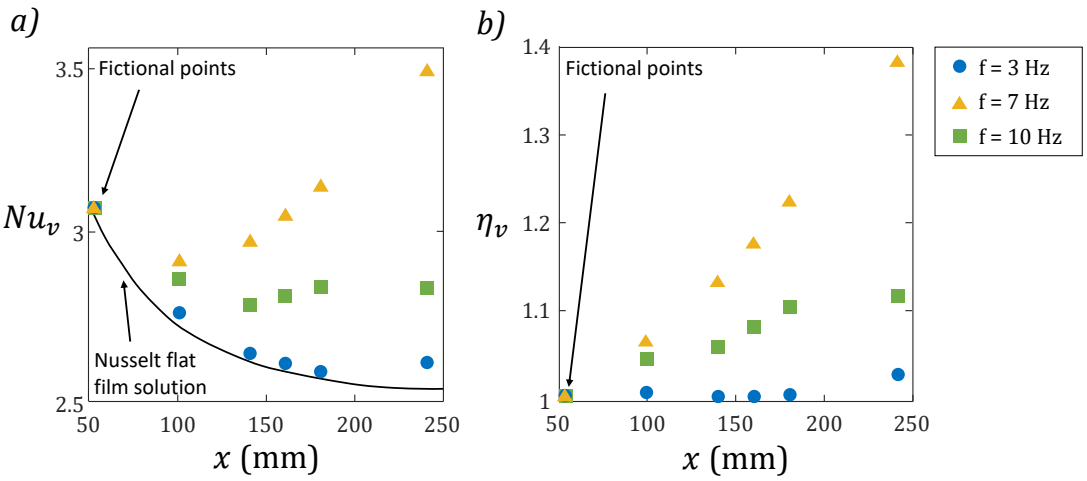


Figure 12: Spatial evolution of the Nusselt number $\overline{\mathrm{Nu}_v}$ (a) and η_v (b) along the liquid film for three perturbation frequencies f for $\mathrm{Re} = 200$, $\beta = 10$ ° and $q_w = 1.25$ W/cm^2. The black line represents the Nusselt flat film solution.

The choice of the temperature $\overline{T_m}$, $\overline{T_s}$, or $\overline{T_v}$ in the evaluation of Nu (Equation 7), is likely to modify the value of the efficiency factor η. Therefore, a comparison is presented hereafter in Figure 13 for the same flow conditions as in Figure 12. Although the Nusselt number takes very different values with these temperatures, the normalization by Nu_0 calculated with the same temperature, results in relatively close values of the efficiency factor η. In particular, the differences are not significant between η_m and η_v. In contrast, using T_s leads to an overestimate of about 10% in the value of η compared to the other two temperatures. The difference may be due to some bias in the measurement of the surface temperature. While T_m, T_v and T_s are all evaluated from the same temperature field obtained with the PLIF technique, a fine positioning of the air/water interface is required to calculate correctly the surface temperature T_s. An average over a large number of pixels is performed to evaluate T_m and T_v, while for the surface temperature measurement, only the pixels close to the liquid surface are

considered. Despite those differences in the evaluation of η, similar conclusions can be drawn using any of the three temperatures in the evaluation of η concerning the effect of the waviness on the heat transfer.

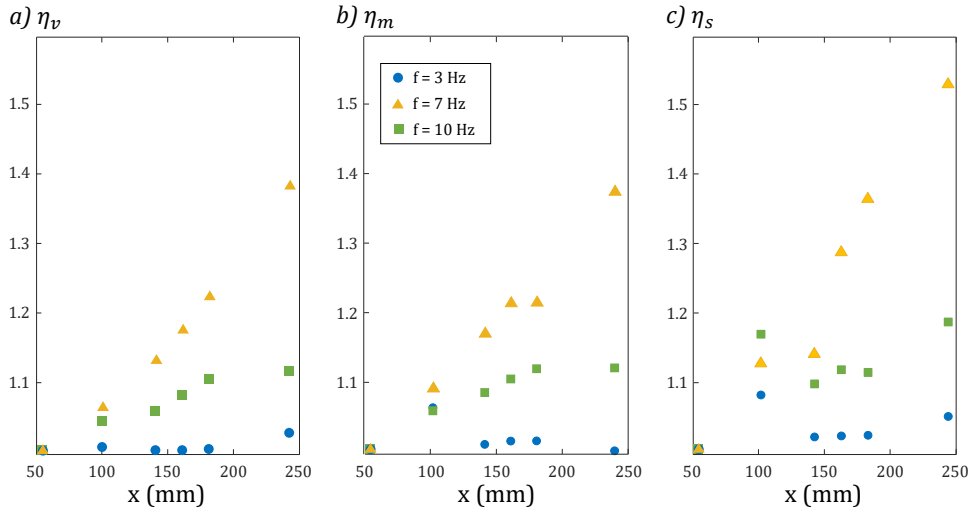


Figure 13: Spatial evolution of the efficiency factor η calculated with the three previously defined film temperature T_m, T_v and T_s. Same experimental conditions as in Fig. 12. As in Fig. 12, the points at $x = 50$ mm were hand placed to help read the trends.

4.2.3 Influence of the Reynolds number

The effect of the Reynolds number can be investigated by modifying the liquid flow rate. In practice, testing a wide range of flow rates proved to be difficult. For the low flow rate, dewetting occurs quite easily on the edge of the liquid film near the electrodes which leads to an extremely fast overheating of the titanium foil and its degradation. For large film thicknesses, temperature variations becomes too small to be measured accurately. Three different values of the Reynolds number corresponding to Re = 150, Re = 200 and Re = 250 were considered in the following results. Figure 14 shows the variation of T_w with the downstream distance x for the considered Re values while β is fixed at 10°. For a fixed heat flux q_w, the temperature difference $(T_w - \overline{T_m})$ is expected to increase as the liquid film is getting thinner. Regardless of the wave frequency f, the higher the liquid flow rate, the smaller is the increase in the wall temperature at the end of the heated wall.

In Figure 15, the dimensionless distance $x^* = x/\left(\overline{\delta} \cdot \mathrm{Pe}\right)$ is introduced for the horizontal axis. This allows measurements of T_w obtained at different values of Re but the same wave frequency to collapse onto the same curves. Hence, the effect of the wave frequency, already illustrated for Re = 200 in Figure 12, remains essentially the same at other values of Re, provided the dimensionless distance x^* is used.

A significant change in the evolution of θ_w^* can be pointed out after $x^* = 0.05$ for $f = 7$ Hz and for slightly higher values of x^* at other wave frequencies. As stated before, these deviations from the Nusselt theory indicate an increase in the heat transfer due to a change in the distribution of the temperature inside the film. As long as x^* is small (typically less than 0.05), the growth of the thermal boundary layer is unaffected by the waves and follows the Nusselt solution. Then, as the top of the thermal boundary layer is approaching the free surface, advective motions induced by the waves start

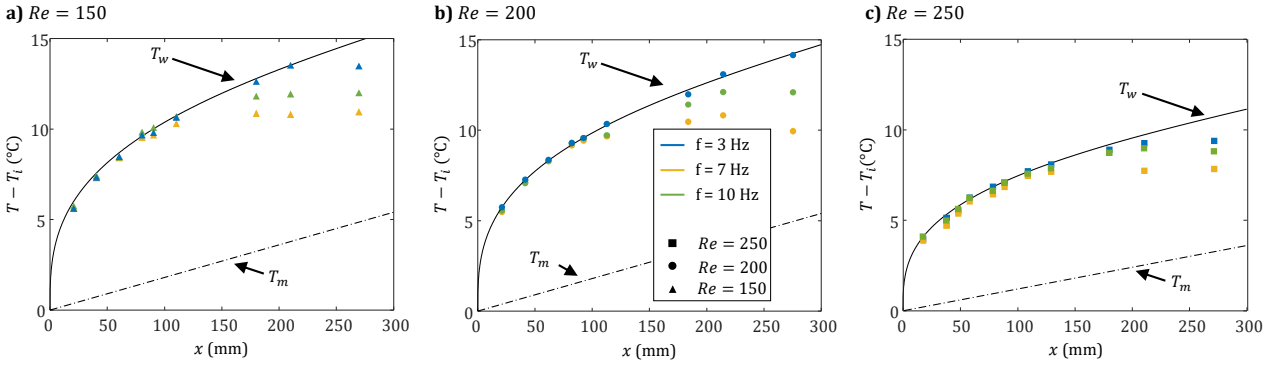


Figure 14: Spatial evolution of the measured wall temperature T_w for three Reynolds numbers Re = 150 (a), Re = 200 (b) and Re = 250 (c) and three perturbation frequencies f = 3 Hz, 5 Hz and 10 Hz, $\beta = 10$ ° and $q_w = 1.25$ W/cm^2.

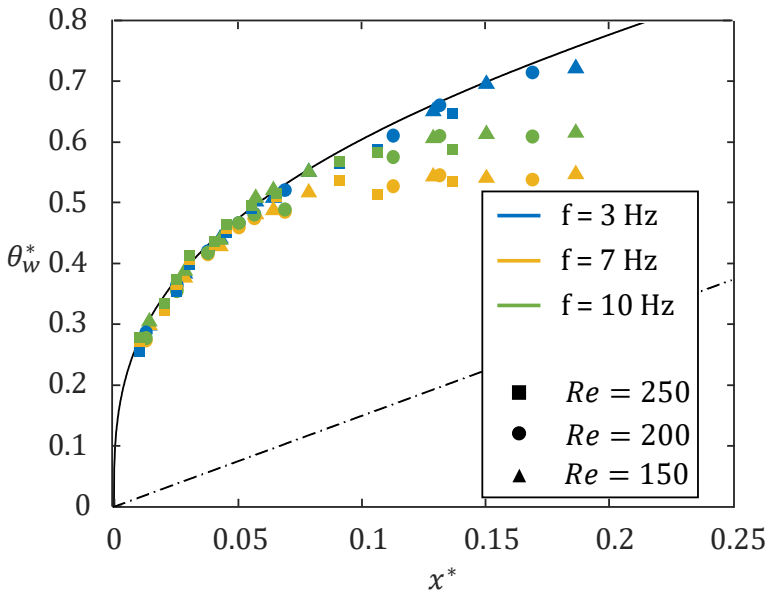


Figure 15: Spatial evolution of the non-dimensional wall temperature θ_w^* for three values of the Reynolds number Re and three perturbation frequencies f as represented on graphs (a), (b) and (c) of Figure 14. The dotted line represents the liquid film temperature θ_m^*.

to play a significant role. For $f = 7$ Hz, waves are characterized by a recirculation zones under the wave crest (Figure A.1), which extends deep inside the liquid film. For the other wave frequencies, the wave height is smaller and these waves are less efficient at generating mixing and advection in the depth of the liquid film. For these reasons, the effect of mixing becomes noticeable at a larger downstream distance.

4.2.4 Influence of the wall inclination

Experiments were also conducted while changing the angle β of the titanium foil relative to the horizontal from 2 ° to 10 °. In Figure 16, the efficiency coefficient η_v is plotted as a function of x^* for a great number of experimental cases corresponding to 150 $\leq$ Re $\leq$ 250, 2°$\leq \beta \leq$ 10 ° and f = 3, 7 or 10 Hz. Despite some scattering, all the experimental data fall on three curves which are consistent with the effect of the wave frequency already described in Section 4.2.2. This suggests that the effects

of both Re and β are well captured by x^*, leaving only the effect of the wave frequency apparent in Figure 16. The main effect of increasing β, is a decrease in the time-averaged film thickness $\overline{\delta}$. Using Equation (1), $\overline{\delta}$ can be expressed as:

$$\overline{\delta} = \left(\frac{\mathrm{Re}}{sin\,(\beta)} \frac{3\nu^2}{g} \right)^{\frac{1}{3}}. \tag{16}$$

The film thickness is included in the expression of the Nusselt number Nu and the dimensionless distance x^* (Equations (3) and (7)).

The fact that the heat transfer is mainly influenced by f and marginally by β in Figure 16 deserves some comments. In the present experiments, the waves are generated in an upper tank completely dissociated from the wall. Also, the length of the wall is not sufficient for the waves to evolve significantly from their initial shape. This results in a film perturbation that is weakly dependent on the angle of inclination but mainly on the wave frequency.

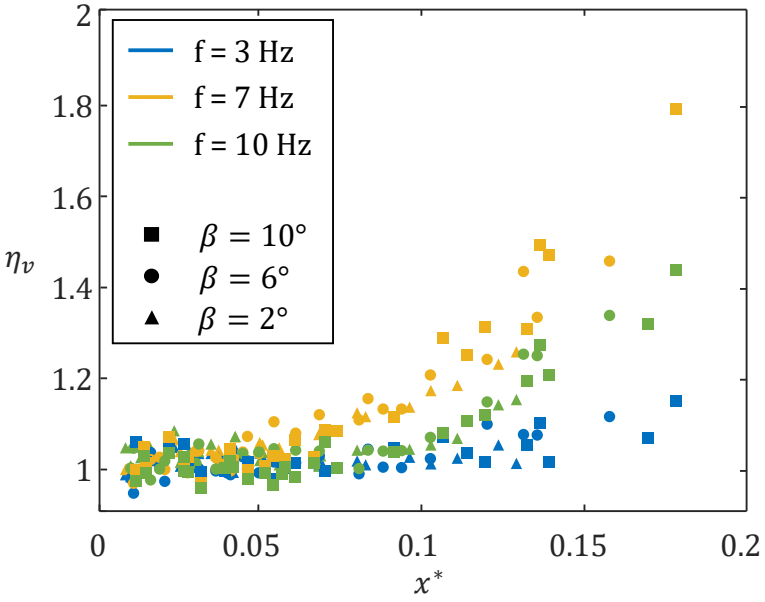


Figure 16: Evolution of the efficiency factor η_v obtained experimentally with the dimensionless distance x^*. The data covers the totality of the studied Re, β and f values.

4.3 Temporally and spatially resolved heat transfer

To gain insights into the fundamental role of advective mixing, more specific approaches are required to obtain both time- and space-resolved information on the inner temperature distribution. The following section deals with the identification of the most active zones in the mixing process. Prior observations of the temperature field inside the waves were reported by Collignon et al. (2021) who developed the PLIF imaging technique also employed in the present study. The authors proposed to group measurements into three main categories to describe the mixing evolution:

1. **Diffusion limited:** The thermal boundary layer is still too thin to interact with the wave, or the amplitude of the waves is too small to generate an efficient perturbation of the thermal boundary

layer. In this situation, the waves have a negligible influence on the temperature distribution which is stratified parallel to the wall every where.

2. **Localized mixing:** The temperature field is mainly stratified, but in some particular regions of the film (for example the crest of the wave, the capillary troughs...) mixing has significantly changed the temperature distribution. This situation is usually a transitional one before a mixing extending more widely inside the film.

3. **Widespread mixing:** The mixing extends to the whole liquid volume. This situation can be observed for the waves with a sufficiently high amplitudes. Although the temperature is not completely homogeneous in the film, mixing has affected all the regions of the film. Temperature stratification has almost completely disappeared.

In the present study, an attempt is made to characterize the mixing on a more quantitative basis. To that end, experimental temperature fields are compared with the Nusselt solution described earlier. In a first stage, the heat equation (4) is solved numerically in the dimensionless coordinates (x^*, z^*) using $\overline{\delta}$ as reference length in the calculation of x^* and z^* (Equation 3). This equation implies a velocity field unperturbated by the waves and a film, which has the same thickness in average. The solution obtained with the boundary conditions (5) is only valid for $0 \leq z^* \leq 1$. To be compared with the experiments, this solution must be extrapolated in the wave humps where $z \geq \overline{\delta}$. In practice, a 2^{nd} order polynomial interpolation is used in order to have no discontinuity of the temperature and the heat flux at the connection in $z^* = 1$. It allows having a zero derivative for the temperature at the film surface. An example of such temperature reconstruction is presented in Figure 17.b for a liquid film corresponding to Re = 200, $\beta = 10$ °, $x = 180$ mm, $f = 10$ Hz and $T_i = 10$ °C, which falls into the above category of a localized mixing. The deviation between the theoretical temperature field derived from the Nusselt solution (denoted T_{Nu}) and the experimental temperature field (denoted T_{exp}), can be used to point out the film regions where mixing has an influence on the temperature distribution. For the example presented in Figure 17, the mixing mainly concerns three regions:

- The capillary trough where a pocket of liquid at a higher temperature can be observed. A mechanism similar to a flow separation pointed out by Dietze and Kneer (2011) can explain the formation of such as a process for enhancing the heat transfer.

- Under the hump of the main wave is a region of colder liquid. The wave hump is known to contain a vortex in the reference frame attached to the wave. In Figure A2, the streamlines obtained for the same wave configuration confirm the presence of a vortex. However, the cold liquid pocket is at a short distance of the wall, which cannot be easily explained by the velocity field given by the Kapitza-Shadov approximation (Equations (17)-(18)-(19)).

- In the inter-wave region (for $0 \leq \varphi \leq 3\pi/4$ and $7\pi/4 \leq \varphi \leq 2\pi$), a layer of slightly warmer liquid is observed at the vicinity of the wall. This region is connected to the even warmer region in the capillary trough mentioned above.

The results suggest a cyclic process where the thermal boundary layer is reset each time there is a interference with the main wave and redevelops then in the inter-wave region.

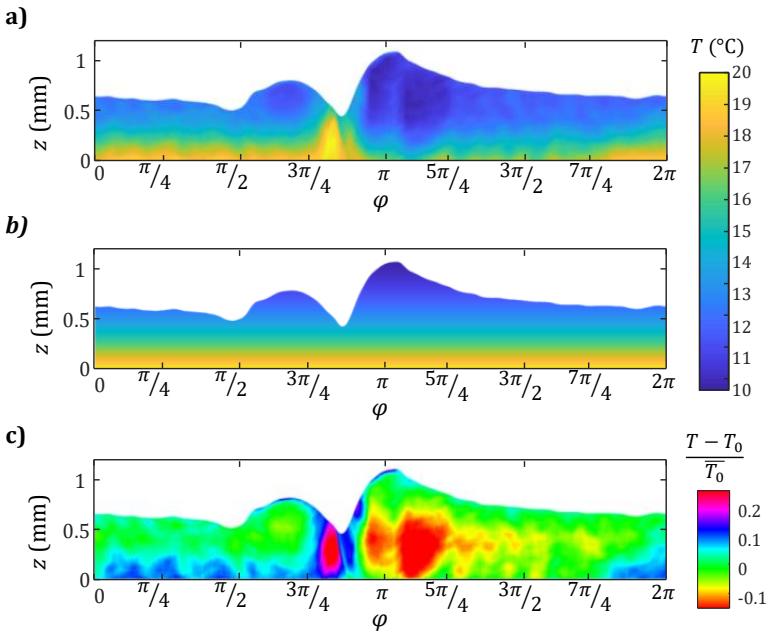


Figure 17: Temperature field T in the film obtained using PLIF measurement technique (a) and the corresponding temperature field T_{Nu} calculated with the extrapolated Nusselt solution under the assumption of pure diffusion in the transverse direction (b). The normalized difference between T and T_{Nu} is shown in (c). Results correspond to Re = 200, $\beta = 10$ °, $x = 180$ mm, $f = 10$ Hz and $T_i = 10$ °C.

Additional images from the same flow configuration are presented in Figure 18. To observe significant deviations from the theoretical Nusselt solution, a distance of about 14 cm was necessary. Images show that the mixing first appears in the capillary trough preceding the main wave and close to the wall under the hump of the main wave. Then, between $x = 140$ mm and 180 mm, the mixing zone gradually grow up. At $x = 180$ mm, the largest differences are found with the Nusselt solution. After $x = 180$ mm, the morphology of the wave evolves drastically with a multiplication of troughs and humps, making the description of the ensuing mixing process particularly difficult. At $x = 240$ mm, the heat transfer from the wall is enhanced by a large colder region of the liquid close to the wall.

The above approach based on a comparison with the Nusselt solution, can also be used to analyze the time-resolved measurements obtained with the LIF probe. The solution of the heat equation (4) is first obtained numerically and then extrapolated up to $z = \delta(x,t)$. Finally, the calculated temperature field is averaged over the film thickness using Equation (9) to calculate the volume-averaged temperature $T_v(x,t)$. In Figure 19, this approach is applied to a film in the same conditions as in Figure 17. The phase φ of the wave is used as a marker color and the extrapolated Nusselt solution is shown as a solid black line. The theoretical model without mixing predicts that the volume-averaged temperature T_v is decreasing monotonically with δ. A good agreement is observed with the measurements except in the capillary trough and in the wave crest. The measured temperature is greater than the Nusselt solution without mixing close to the capillary trough, while it is lower in the wave crest region. Hence, the results presented in Figure 19 are consistent with previous observations made using PLIF images (Figure 17.c).

The method was therefore applied to other flow configurations obtained for $f = 3$ Hz and $f = 7$ Hz, which are presented in Figures 20 and 21. In these figures, the evolution of the heat transfer coefficient

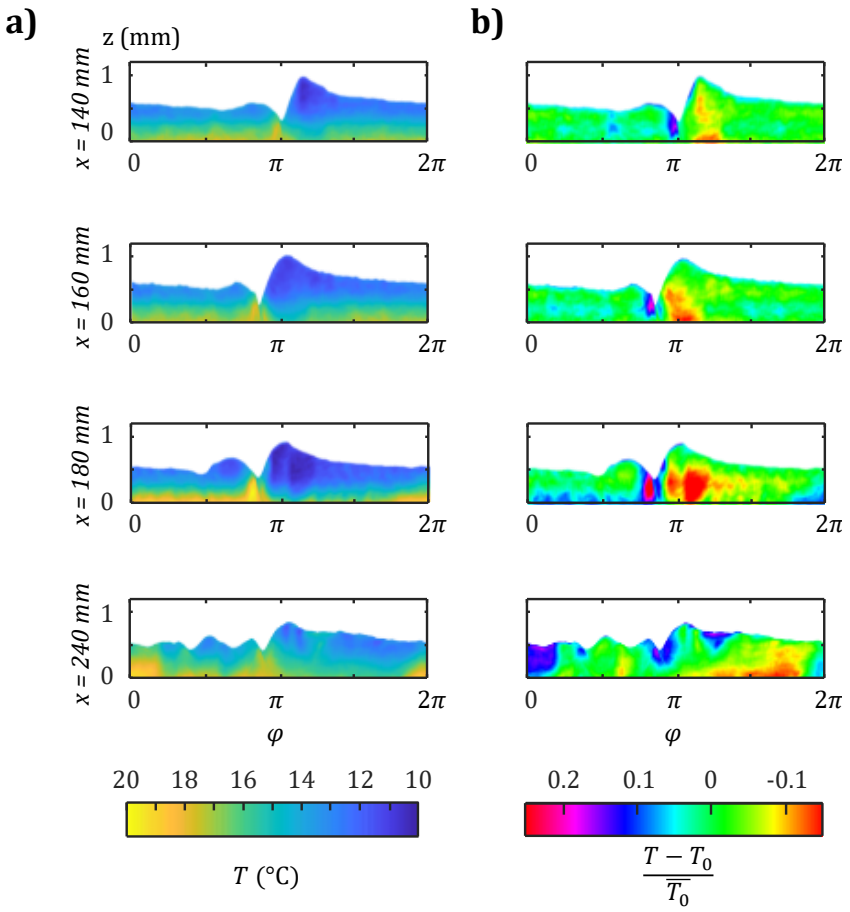


Figure 18: Spatial evolution of the temperature field T (a) and of the normalized difference between T and T_{Nu} (b) along the flow of the film. Results were obtained for Re = 200, $\beta = 10$ °, $f = 10$ Hz and $T_i = 10$ °C.

h_v, defined by $h_v = q_w/(T_w - T_v)$, is shown. A good agreement between the extrapolated Nusselt solution and the experimental data, can be observed for $f = 3$ Hz (Figure 20.b), which was expected given the low mixing capability of this wave frequency. The wave amplitude slightly increases with the distance x (Figure 20.a), but the amplification is too limited to generate an efficient mixing. It induced a small increase of the heat transfert coefficient h_v during the wave period but the deviation from the extrapolated Nusselt solution remains negligible. In Figure 20, the time average heat transfer coefficient $\overline{h_v}$ is indicated by a horizontal dashed line. The time-averaged heat transfer coefficient $\overline{h_v}$ decreases progressively with the distance x, as it was already observed for the Nusselt number $\overline{\mathrm{Nu}_v}$ in Figure 11.

For the frequency $f = 7$ Hz, the situation depicted in Figure 21, is quite different. At $x = 60$ mm, the agreement with the extrapolated Nusselt solution is good almost everywhere except very locally in the capillary trough preceding the main wave. Then, the discrepancy with the model gradually extends to more regions as the wave profile also evolves. The regions marked in red, which correspond to the capillary trough and the wave front, are the places where the biggest differences can be found with the extrapolated Nusselt solution. The region of the wave crest (in dark red) is characterized by the lowest values of heat transfer coefficient h_v. As illustrated in Figure 17 for the frequency $f = 10$ Hz, a pocket of cold liquid can be suspected in the wave hump due to liquid recirculation, resulting in a larger difference $(T_w - T_v)$ than anywhere else in the film. For $x \geq 240$ mm, the temperature is getting

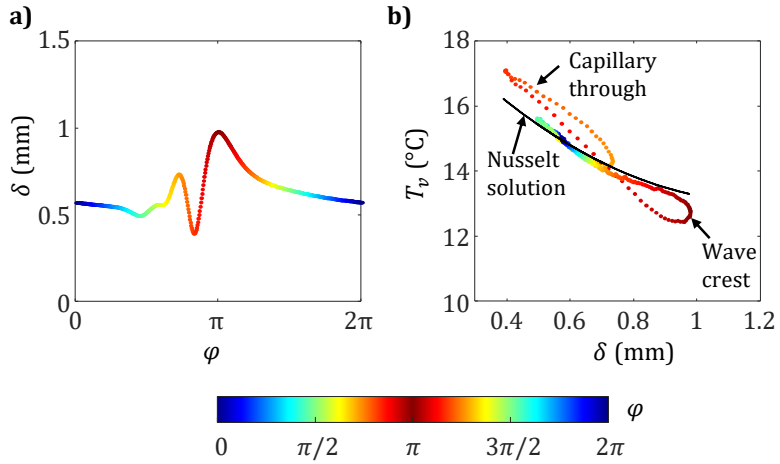


Figure 19: Evolution of the thickness δ (a) and the volume average temperature T_v (b) during the period of a wave. The conditions correspond to $f = 10$ Hz, Re $= 200$, $\beta = 10$ °, $T_i = 10$ °C and $q_w = 1.25$ W/cm^2 and $x =$180 mm. The black curve is for the theoretical model based on the Nusselt solution which allows to determine the average temperature in the film cross-section in the absence of mixing by the wave.

more homogeneous in the film due to the mixing. The experimental volume-averaged temperature T_v deviates from the extrapolated Nusselt solution in almost every region (widespread mixing). For $x = 270$ mm, the effects of the mixing are even more visible. As a result of a uniform temperature, the curve featuring h_v as a function of δ is flattened almost horizontally in Figure 20. Only the top of the wave is still having a slightly lower temperature than the film average. When compared to the extrapolated Nusselt solution (black curve), the heat transfer coefficient h_v has increased everywhere due to the mixing except for the points in blue but the differences are quite limited for them. While the time-averaged heat transfer coefficient $\overline{h}_v$ is continuously decreasing with x for $f = 3$ Hz, it remains at a value close to 2000 W/m^{2}K for $f = 7$ Hz as a result of the heat transfer enhancement.

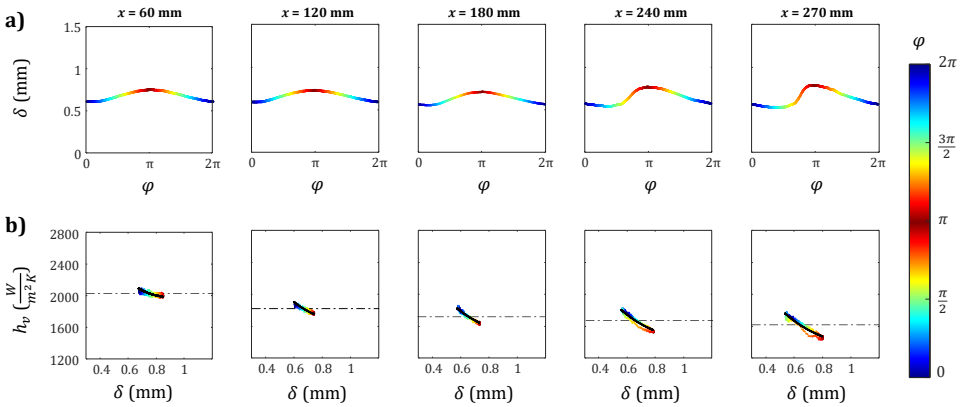


Figure 20: Evolution of the thickness δ (a) and the heat transfer coefficient h_v (b) of the falling liquid film compared to the pure diffusion model (black line). The color of the curves is matched in phase between the two rows. The horizontal dotted line is the time average heat transfer coefficient calculated from the experimental data from the LIF probe. Results for $f = 3$ Hz, Re $= 200$, $\beta = 10$ °, $T_i = 10$ °C and $q_w = 1.25$ W/cm^2.

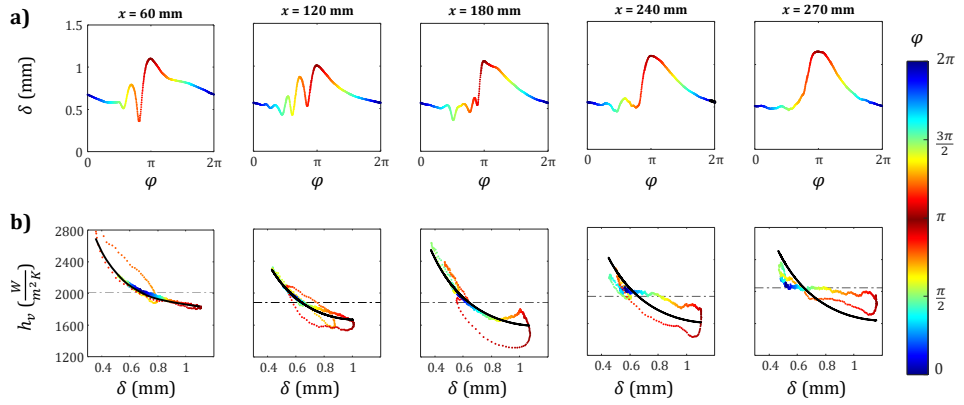


Figure 21: Evolution of the thickness δ (a) and the heat transfer coefficient h_v (b) of the falling liquid film compared to the pure diffusion model (black line). The color of the curves is matched in phase between the two rows. The horizontal dotted line is the time average heat transfer coefficient calculated from the experimental data from the LIF probe. Results for $f = 7$ Hz, Re $= 200$, $\beta = 10$ °, $T_i = 10$ °C and $q_w = 1.25$ W/cm^2.

5 Conclusions

Using different optical arrangements, the two-color laser-induced fluorescence technique can provide either planar measurements of the temperature field within wavy liquid films or pointwise measurements of the temperature averaged over the film thickness. The combination of theses measurements with those of the film height, and of the wall temperature, provides valuable data for quantifying heat transfer via the heat transfer coefficient and thus, the Nusselt number.

From the temperature field measurements, it has been observed that a variety of possible definitions of the heat transfer coefficient, derived from different experimental and theoretical methods developed in the community, are comparable and capture the main trends of the temperature and heat transfer.

A comparison with the Nusselt solution, which considers pure diffusive heat transfer in the direction

perpendicular to the flow within a flat film, can be used to evaluate the time-averaged increase in heat transfer trough wave-induced mixing inside wavy films. A critical wave height and distance from the flow inlet are required to observe significant deviation of the thermal boundary layer compared to the Nusselt solution, which develops over the heated wall. Waves with the most pronounced crests and capillary troughs are the most efficient in terms of promoting thermal mixing. The effects of both the Reynolds number and of the wall inclination can be accounted for by introducing a dimensionless distance and a normalized temperature, calculated based on the time-averaged film thickness.

Assuming a spatial extrapolation of the Nusselt solution up to the wave crests, it is also possible to identify regions where the mixing induces a significant change in temperature (up to 25%). The method can be applied for comparison with experimental temperature images, or with the volume-averaged temperature measurements, even if the analysis is less straightforward in that case. Results reveal that the mixing starts from the main capillary troughs and close to the wall just below the hump of the main wave and then, progressively extents and spreads to other film regions. The consequence of this mixing is a reduction in the variation of the heat transfer coefficient between the crest of the wave and the capillary trough from 40% at the inlet of the flow to 20% at the end of the plate.

Acknowledgments

The authors acknowledge support by the FRAISE project, grant ANR-16-CE06-0011 of the French National Research Agency (ANR).

References

A. Miyara, Numerical analysis on flow dynamics and heat transfer of falling liquid films with interfacial waves, Heat and Mass Transfer 35 (1999) 298–306. doi:10.1007/s002310050328.

E. A. Demekhin, E. N. Kalaidin, S. Kalliadasis, S. Y. Vlaskin, Three-dimensional localized coherent structures of surface turbulence. i. scenarios of two-dimensional–three-dimensional transition, Physics of Fluids 19 (2007) 114103. doi:10.1063/1.2793148.

G. F. Dietze, A. Leefken, R. Kneer, Investigation of the backflow phenomenon in falling liquid films, Journal of Fluid Mechanics 595 (2008) 435–459. doi:10.1017/S0022112007009378.

C. Albert, A. Tezuka, D. Bothe, Global linear stability analysis of falling films with inlet and outlet, Journal of Fluid Mechanics 745 (2014) 444–486. doi:10.1017/jfm.2014.57.

M. Chhay, D. Dutykh, M. Gisclon, C. Ruyer-Quil, New asymptotic heat transfer model in thin liquid films, Applied Mathematical Modelling 48 (2017) 844 – 859. doi:10.1016/j.apm.2017.02.022.

H. Yu, T. Gambaryan-Roisman, P. Stephan, Numerical Simulations of Hydrodynamics and Heat Transfer in Wavy Falling Liquid Films on Vertical and Inclined Walls, Journal of Heat Transfer 135 (2013). doi:10.1115/1.4024550.

C. N. Markides, R. Mathie, A. Charogiannis, An experimental study of spatiotemporally resolved heat transfer in thin liquid-film flows falling over an inclined heated foil, International Journal of Heat and Mass Transfer 93 (2016) 872 – 888. doi:10.1016/j.ijheatmasstransfer.2015.10.062.

O. A. Kabov, B. Scheid, I. A. Sharina, J.-C. Legros, Heat transfer and rivulet structures formation in a falling thin liquid film locally heated, International Journal of Thermal Sciences 41 (2002) 664 – 672. doi:10.1016/S1290-0729(02)01361-3.

A. Charogiannis, F. Denner, B. G. M. van Wachem, S. Kalliadasis, C. N. Markides, Detailed hydrodynamic characterization of harmonically excited falling-film flows: A combined experimental and computational study, Phys. Rev. Fluids 2 (2017) 014002. doi:10.1103/PhysRevFluids.2.014002.

F. Denner, A. Charogiannis, M. Pradas, C. N. Markides, B. G. M. van Wachem, S. Kalliadasis, Solitary waves on falling liquid films in the inertia-dominated regime, Journal of Fluid Mechanics 837 (2018) 491–519. doi:10.1017/jfm.2017.867.

N. Brauner, D. Marón, Modeling of wavy flow in inclined thin films, Chemical Engineering Science 38 (1983) 775–788. doi:10.1016/0009-2509(83)80187-0.

R. Roberts, H.-C. Chang, Wave enhanced interfacial transfer, Chemical Engineering Science 55 (2000) 1127–1141. doi:10.1016/S0009-2509(99)00391-7.

A. Rastaturin, E. Demekhin, E. Kalaidin, Optimal regimes of heat-mass transfer in a falling film, Journal of Non-Equilibrium Thermodynamics 31 (2006) 1–10. doi:doi:10.1515/JNETDY.2006.001.

D. Gao, N. B. Morley, V. K. Dhir, Numerical simulation of wavy falling film flow using vof method, Journal of Computational Physics 192 (2003) 624–642.

G. Zhou, A. Prosperetti, Capillary waves on a falling film, Phys. Rev. Fluids 5 (2020) 114005. doi:10.1103/PhysRevFluids.5.114005.

G. Dietze, R. Kneer, Flow separation in falling liquid films, Frontiers in Heat and Mass Transfer 2 (2011). doi:10.5098/hmt.v2.3.3001.

J. Tihon, K. Serifi, K. Argyriadi, V. Bontozoglou, Solitary waves on inclined films: their characteristics and the effects on wall shear stress, Experiments in Fluids 41 (2006) 79–89. doi:10.1007/s00348-006-0158-1.

A. Schagen, M. Modigell, G. Dietze, R. Kneer, Simultaneous measurement of local film thickness and temperature distribution in wavy liquid films using a luminescence technique, International Journal of Heat and Mass Transfer 49 (2006) 5049 – 5061. doi:10.1016/j.ijheatmasstransfer.2006.06.010.

S. W. Joo, S. H. Davis, S. G. Bankoff, A mechanism for rivulet formation in heated falling films, Journal of Fluid Mechanics 321 (1996) 279–298. doi:10.1017/S0022112096007720.

D. V. Zaitsev, O. A. Kabov, Study of the thermocapillary effect on a wavy falling film using a fiber optical thickness probe, Experiments in Fluids 39 (2005) 712–721. doi:10.1007/s00348-005-0003-y.

R. Collignon, O. Caballina, F. Lemoine, G. Castanet, Temperature distribution in the cross section of wavy and falling thin liquid films, Experiments in Fluids 62 (2021) 115. doi:10.1007/s00348-021-03175-x.

R. Collignon, O. Caballina, F. Lemoine, G. Castanet, Simultaneous temperature and thickness measurements of falling liquid films by laser-induced fluorescence, Experiments in Fluids 63 (2022) 68. doi:10.1007/s00348-022-03420-x.

E. J. Davis, Exact solutions for a class of heat and mass transfer problems, The Canadian Journal of Chemical Engineering 51 (1973) 562–572. doi:10.1002/cjce.5450510506.

A. N. Chernyavskiy, A. N. Pavlenko, Numerical simulation of heat transfer and determination of critical heat fluxes at nonsteady heat generation in falling wavy liquid films, International Journal of Heat and Mass Transfer 105 (2017) 648–654. doi:10.1016/j.ijheatmasstransfer.2016.09.017.

Y. Wan, C. Ren, L. Xing, Y. Yang, Analysis of heat and mass transfer characteristics in vertical plate channels with falling film evaporation under uniform heat flux/uniform wall temperature boundary conditions, International Journal of Heat and Mass Transfer 108 (2017) 1279 – 1284. doi:10.1016/j.ijheatmasstransfer.2016.12.110.

F. Huaylla, B. Stutz, N. L. Pierrès, Numerical and experimental analysis of falling-film exchangers used in a libr–h2o interseasonal heat storage system, Heat Transfer Engineering 40 (2019) 879–895. doi:10.1080/01457632.2018.1446850.

V. Shkadov, Wave flow regimes of a thin layer of viscous fluid subject to gravity, Fluid Dynamics 2 (1967) 29–34. doi:10.1007/BF01024797.

E. A. Chinnov, E. N. Shatskii, O. A. Kabov, Evolution of the temperature field at the three-dimensional wave front in a heated liquid film, High Temperature 50 (2012) 98–105. doi:10.1134/S0018151X12010038.

R. Mathie, H. Nakamura, C. N. Markides, Heat transfer augmentation in unsteady conjugate thermal systems – part ii: Applications, International Journal of Heat and Mass Transfer 56 (2013) 819 – 833. doi:10.1016/j.ijheatmasstransfer.2012.09.017.

E. A. Chinnov, S. S. Abdurakipov, Influence of artificial disturbances on characteristics of the heated liquid film, International Journal of Heat and Mass Transfer 113 (2017) 129 – 140. doi:10.1016/j.ijheatmasstransfer.2017.05.064.

A. Charogiannis, J. S. An, C. N. Markides, A simultaneous planar laser-induced fluorescence, particle image velocimetry and particle tracking velocimetry technique for the investigation of thin liquid-film flows, Experimental Thermal and Fluid Science 68 (2015) 516 – 536. doi:10.1016/j.expthermflusci.2015.06.008.

A. Charogiannis, C. N. Markides, Spatiotemporally resolved heat transfer measurements in falling liquid-films by simultaneous application of planar laser-induced fluorescence (PLIF), particle tracking velocimetry (PTV) and infrared (IR) thermography, Experimental Thermal and Fluid Science 107 (2019) 169 – 191. doi:10.1016/j.expthermflusci.2018.11.001.

J. Sakakibara, R. Adrian, Whole field measurement of temperature in water using two-color laser induced fluorescence, Experiments in Fluids 26 (1999) 7–15. doi:10.1007/s003480050260.

W. Chaze, O. Caballina, G. Castanet, F. Lemoine, Spatially and temporally resolved measurements of the temperature inside droplets impinging on a hot solid surface, Experiments in Fluids 58 (2017). doi:10.1007/s00348-017-2375-1.

M. Stiti, A. Labergue, F. Lemoine, S. Leclerc, D. Stemmelen, Temperature measurement and state determination of supercooled droplets using laser-induced fluorescence, Experiments in Fluids 60 (2019). doi:10.1007/s00348-018-2672-3.

W. Chaze, O. Caballina, G. Castanet, F. Lemoine, The saturation of the fluorescence and its consequences for laser-induced fluorescence thermometry in liquid flows, Experiments in Fluids 57 (2016) 58. doi:10.1007/s00348-016-2142-8.

F. Al-Sibai, A. Leefken, U. Renz, Local and instantaneous distribution of heat transfer rates through wavy films, International Journal of Thermal Sciences 41 (2002) 658 – 663. doi:10.1016/S1290-0729(02)01360-1.

A Appendix

A.1 Calculation of the velocity field within a wave using the Kapitza-Shkadov model

In order to evaluate the local temperature weighted by the local flow T_m from the PLIF temperature field, the velocity field can be calculated from the thickness profile measurement using the Kapitza-Skadov model (Shkadov, 1967). The tangential and normal components of the velocity relative to the wall, respectively u and w, are based on the following set of equations:

$$\frac{\partial \delta}{\partial t} + \frac{\partial \Gamma}{\partial x} = 0, \tag{17}$$

$$u = \frac{3\Gamma}{\delta}\left(\frac{z}{\delta} - \frac{1}{2}\frac{z^2}{\delta^2}\right), \tag{18}$$

$$w = -\int_0^{\delta} \frac{\partial u}{\partial x} dz, \tag{19}$$

where $\Gamma = q_v/l$ is the spectific flow rate in the considered cross-section of thickness δ. The Kapitza-Shkadov model assumes that the velocity field is always parabolic and purely laminar at any time and any position in the film. In order to calculate $T_m(x)$ from Equation (8), the local value of the temperature at position (x, y) is evaluated using the PLIF temperature images, while the time variations of δ is obtained directly from the wave profile on the PLIF images. One example of velocity field calculated with this approach is presented in Figure A.1 where the black lines are the stream lines in the frame of the wave. This example corresponds to the same flow configuration as in Figure 17. In the reference frame linked to the wave, a vortex can be seen in the main hump of the wave. Its location matches rather well with the region of lower temperature measured by PLIF. In contrast, the Kapitza-Shkadov model can hardly explain the ascending hot liquid observed in the trough that precedes the main wave.

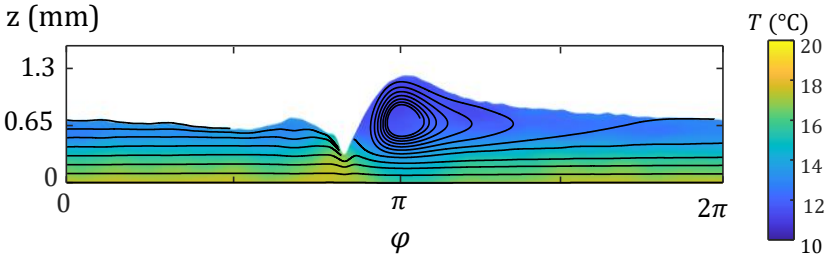


Figure A.1: Stream lines of the flow in the liquid film under a wave obtained using the Kapitza-Shkadov model used for the velocity calculation, printed over the temperature field measured by PLIF. Results for Re = 200, $\beta = 10°$, $f = 10$ Hz, $x = 160$ mm, $T_i = 10°$C and $q_w = 1.25$ W/cm^2

A.2 Evaluation of the time-averaged Nusselt number

The film temperature and the film thickness are measured simultaneously with either the LIF probe or PLIF imaging. From those measurements, the time averaged Nusselt number Nu can be evaluated in two different ways depending whether time average is applied prior to the different terms in the expression of the Nusselt number or to the Nusselt number itself:

$$\overline{Nu_{v,1}} = \frac{q_w}{\lambda} \frac{\overline{\delta}}{\overline{T_v - T_w}} \tag{20}$$

$$\overline{Nu_{v,2}} = \frac{q_w}{\lambda} \overline{\left(\frac{\delta}{T_v - T_w} \right)} \tag{21}$$

In order to compare these two methods, the calculations of the time-averaged Nusselt number where compared for two cases of liquid films perturbation frequency. In the first liquid film, the waves are generated at a frequency $f = 7$ Hz and they have a relatively high height. While in the second case, the wave frequency of 3 Hz leads to a low wave height (Figure 8). As it can be seen in Figure A.2, the curves associated with the two methods are hardly distinguishable.

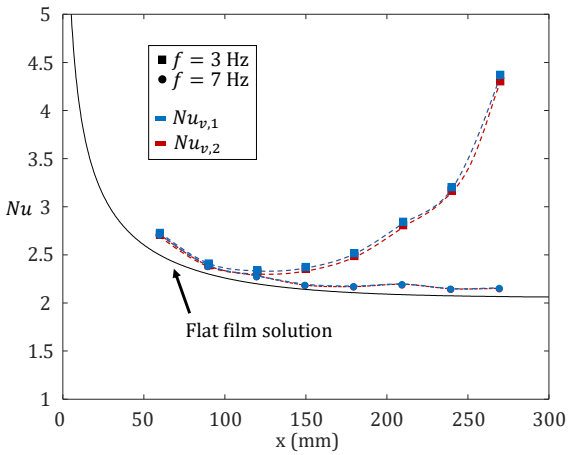


Figure A.2: Comparison of the two time-averaging methods used to evaluate the Nusselt number. The first method based on Equation (20) is plotted in blue, while the second method based on Equation (21) is plotted in red. The results correspond to two wave frequencies ($f = 3$ Hz and $f = 7$ Hz) and were obtained for Re $= 200$, $\beta = 10°$ and $q_w = 1.25$ W/cm^2.